Improvement of Sea Ice Drift Extraction Based on Feature Tracking from C-SAR/01 Imagery

Yanli Yang , Tao Xie , Chengzhi Sun, Chao Wang , Jian Li , and Xuehong Zhang

Abstract—In this study, the extraction of sea ice drift from imagery captured by the 1-meter C-SAR 01 satellite (C-SAR/01) was facilitated utilizing the oriented fast and rotated brief algorithm within the feature tracking procedure, thus addressing the previously unexplored area of sea ice drift extraction using C-SAR/01 imagery. The retained keypoints and nearest neighbor distance ratio test for sea ice drift extracted from C-SAR/01 imagery were compared, indicating high reliability with 300 000 and 0.75, respectively. In addition, the local outlier factor algorithm is proposed in this article, which can effectively remove erroneous sea ice drift vectors. The sea ice drift extracted from C-SAR/01 was validated against manually extracted sea ice drift, revealing an uncertainty of 0.271 cm/s in speed and 8.331° in direction. Furthermore, the sea ice drift obtained from the algorithm in this study, when compared with sea ice drift from IABP buoys, exhibits high accuracy, reflecting the robustness of the algorithm.

Index Terms—1-meter C-SAR 01(C-SAR/01), Arctic, feature tracking (FT), oriented fast and rotated brief (ORB), sea ice drift, synthetic aperture radar (SAR).

I. Introduction

ACCORDING to the Arctic Climate Report 2022, extreme warming events in the Arctic are occurring more frequently, accompanied by accelerated melting of the Greenland ice sheet and an overall decrease in the extent of Arctic sea ice [1]. Sea ice movement serves as an indicator of Arctic Sea ice variability and is an important influencing factor in the overall balance of Arctic Sea ice mass [2], [3]. As for the newly opened shipping routes in the Arctic ice region due to global warming in recent years, enhancing real-time monitoring and numerical forecasting capabilities of sea ice movement is of utmost importance. Therefore, research on sea ice drift plays a prominent role in Arctic climate and environmental studies, Arctic shipping safety, and marine economic activities.

Sea ice movement refers to the complex motion of sea ice driven by various factors such as wind, tides, and ocean currents [4], [5]. The main typical methods used in sea ice drift research include numerical simulations [6], [7], buoy observations [8], satellite remote sensing [9], radar imagery [10], and digital image monitoring [11]. Currently, obtaining wide-ranging sea ice movement data using satellite information has become the primary method due to the advantages of broad observation coverage, rapid imaging, and periodic observations. Satellite sensors that provide sea ice movement research data mainly include passive microwave [12], [13], [14], optical [15], [16], [17], and synthetic aperture radar (SAR) [18], [19], [20], [21], [22], [23], [24] imagery. Currently, the main sea ice movement products published by leading international institutions include National Snow and Ice Data Center (NSIDC), Ocean and Sea Ice Satellite Application Facility, and French Research Institute for the Exploitation of the Seas. However, their spatial resolutions are generally low (6.25–25 km), with average errors ranging from 1–2 km/day and average drift direction errors at 15°–20° [25]. The advantage of microwave radiometers is their broad coverage, allowing for the stitching of data over the entire polar region on a daily basis. However, the disadvantage is their low spatial resolution, typically ranging from a few kilometers to tens of kilometers. In fact, the resolution of remote sensing data is a major factor affecting sea ice information extraction [26]. In comparison, SAR imaging is not affected by weather and illumination conditions, and it has high spatial resolution ranging from a few meters to several hundred meters. Under fine modes, the resolution can reach as high as 1 m. Backscatter coefficients from different polarimetric images exhibit some differences. Studies have shown that the extraction of sea ice drift vectors from HV-polarized images provides more information compared to HH-polarized images [27], [28]. However, HH-polarized images can provide more information on small-scale sea ice variations, yielding more corner features, while HV-polarized images can reflect large-scale ice conditions [29]. China's first civilian C-band high-resolution SAR satellite, GF-3 (Gaofen-3), is equipped with 12 imaging modes [30], [31]. The sea ice drift vectors derived from GF-3 imagery demonstrated a

Yanli Yang, Chengzhi Sun, Jian Li, and Xuehong Zhang are with the School of Remote Sensing and Geomatics Engineering, Nanjing University of Information Science and Technology, Nanjing 210044, China (e-mail: 202211540003@nuist.edu.cn; sunchengzhi@cgs.gov.cn; 003233@nuist.edu.cn; zxhbnu@126.com).

Tao Xie is with the School of Remote Sensing and Geomatics Engineering, Nanjing University of Information Science and Technology, Nanjing 210044, China, also with the Laboratory for Regional Oceanography and Numerical Modeling, Qingdao Marine Science and Technology Center, Qingdao 266200, China, also with the Technology Innovation Center for Integration Applications in Remote Sensing and Navigation, Ministry of Natural Resources, Nanjing 210044, China, and also with the Jiangsu Province Engineering Research Center for Collaborative Navigation/Positioning and Smart Application, Nanjing 210044, China (e-mail: xietao@nuist.edu.cn).

Chao Wang is with the School of Electronics and Information Engineering, Nanjing University of Information Science and Technology, Nanjing 210044, China (e-mail: chaowang@nuist.edu.cn).

high level of accuracy, with uncertainties in speed ranging from 0.119 to 0.287 cm/s, and in direction ranging from 4.119° to 5.930° [32]. The launch of C-SAR/01, a pivotal component of China's SAR satellite network, Launched on November 23rd, 2021. C-SAR/01, as the premier successor to GF-3, has been strategically engineered to advance China's sea and land surveillance capabilities through the establishment of a C-band SAR satellite constellation. So far, there have been no reports on using C-SAR/01 imagery to obtain sea ice drift vectors.

The methods for extracting sea ice drift vectors based on remote sensing image matching mainly include the pattern matching algorithm and the feature tracking (FT) algorithm. The pattern-matching algorithm is simple in principle, has high accuracy, but lacks robustness against rotated sea ice, is sensitive to image noise, and has low computational efficiency [33]. The sea ice drift products mentioned earlier, are all based on the pattern-matching algorithm [34], [35], [36], [37]. FT involves detecting feature points in both the primary and secondary images, such as edge points, corner points, and region extrema. Compared to the pattern matching algorithm, FT algorithms are more computationally efficient, robust against rotated sea ice, but have a higher matching error rate [25]. Typical FT algorithms include scale invariant feature transform, speeded up robust features, accelerated-KAZE, and oriented fast and rotated brief (ORB) [38]. Among them, research has shown that the ORB algorithm exhibits good robustness in sea ice drift vector calculations among several typical algorithms [13]. The ORB algorithm has improved computational efficiency and time complexity. It generates a low-resolution image through the down-sampling method to build an image pyramid for scale invariance and uses a simple and fast algorithm to mark feature points in the image [39]. Muckenhuber et al. [27] applied the ORB operator to extract sea ice drift vectors from Sentinel-1 SAR imagery and improved computational efficiency. Li et al. [32] improved the uniformity of feature points extracted by ORB compared to ORB by adding a Quadtree retrieval method; they eliminated the concentration of feature points extracted by ORB on ice ridges, leads, and coastlines, providing favorable conditions for the subsequent feature point matching calculation. Furthermore, some studies have focused on improving error filtering methods after calculating sea ice drift vectors using the ORB operator [40], [41]. With the increase in remote sensing data sources and high spatial resolution, most researchers have shifted their focus to FT methods.

This article aims to address the issue of uneven spatial distribution in sea ice drift vector calculations using the ORB FT algorithm, utilizing domestically developed SAR satellites, and improving the matching accuracy to some extent. In this study, the ORB method is applied to the C-SAR/01 series images, and the performance of ORB algorithm factors is compared to determine the most suitable algorithm for extracting sea ice drift vectors. Furthermore, we compared NRCS and PR features to find the optimal features to retrieve high-density sea ice drift vectors. To validate the robustness and effectiveness of sea ice drift extraction based on the ORB FT algorithm proposed in this article, both C-SAR/01 data and Sentinel-1 EW data, which exhibits similar performance to C-SAR/01 SAR data,
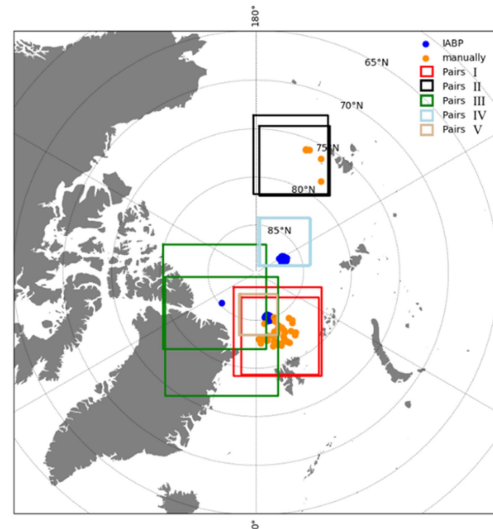

Fig. 1. Geographical positions and the extent of the imagery analyzed in this research. For the C-SAR/01 imagery, Pairs I are denoted by the red rectangle, Pairs II are denoted by the black rectangle, Pairs III are denoted by the green rectangle; for the Sentinel-1 imagery, Pairs IV are denoted by the light-blue rectangle, and Pairs V are indicated with a tan rectangle; and blue dots orange dots on the map serve as markers for the IABP buoy positions and manually extracted sea ice drift used in the study, respectively.

were employed for extracting sea ice drift vectors. The resulting sea ice drift vectors extracted from SAR images were validated against sea ice drift extracted by manually chosen and IABP buoy data.

II. DATA

A. C-SAR/01 Images

China's space infrastructure strategy includes the C-SAR/01 satellite, which utilizes a C-band SAR system with a central frequency of 5.4 GHz. This system is versatile, featuring 12 distinct imaging modes including strip, scan, spotlight, and wave imaging mode [42]. Capable of capturing SAR imagery with resolutions ranging from 1 to 500 m and a coverage swath from 10 to 650 km, the satellite supports configurations from single to full polarization. Terrain observation with progressive scanSAR (TOPSAR) is a novel wide-swath imaging mode for SAR systems. Hence, level-2 images acquired in TOP wide swath (TOPW) mode were selected as data sources for sea ice drift extraction. These images had a resolution of 100 m, a swath width of 500 km, and selective dual-polarization. Considering that the time interval between image pairs used for sea ice drift vector extraction and the speed of motion of sea ice in the covered area affect the results of sea ice drift vector extraction, C-SAR/01 image pairs were selected that were acquired for different time intervals, regions, and seasons. The location and acquisition time of the selected C-SAR/01 images are shown in Table I and Fig. 1.

B. Sentinel-1 Images

The Sentinel-1 constellation contains Sentinel-1A and Sentinel-1B, C-band SAR satellites. The satellite operates in near-polar and sun-synchronous orbits, with the revisit period

TABLE I
DETAIL INFORMATION FOR IMAGES

Satellite	No.	Mode	Pixel size (meter)	Image level	Date of imaging (YY-MM-DD)		Polarization mode	Span(d)
					Image 1	Image 2		
C-SAR/01	Pairs I	TOPW	100	L2	2023-04-06|07:07:47	2023-04-08|07:23:14	HHHV	2
C-SAR/01	Pairs II	TOPW	100	L2	2023-03-24|06:01:37	2023-03-29|05:52:30	HHHV	5
C-SAR/01	Pairs III	TOPW	100	L2	2023-04-07|18:02:00	2023-04-10|17:37:12	HHHV	3
Sentinel-1	Pairs IV	EW	40	L1A	2020-01-02|03:27:29	2020-01-03|04:08:26	HHHV	1
Sentinel-1	Pairs V	EW	40	L1A	2020-04-01|11:40:43	2020-04-02|12:21:40	HHHV	1

in the high-latitude Arctic region can be shortened to 1–2 days, which is conducive to the monitoring of sea ice drift in the Arctic region. This study utilized ground range images obtained from Sentinel-1 in the extra wide swath (EW) mode, possessing a spatial resolution of 40 m. The EW SAR data utilized the TOPSAR imaging technique to provide extensive area coverage. Table I and Fig. 1 provide the information and locations of the Sentinel-1 images. The Sentinel-1 data can be readily accessed online.[1]

C. IABP Buoy Data

The buoy, affixed to the ice surface and moving synchronously with the drifting ice. The buoy data utilized in this study originate from the International Arctic Buoy Program (IABP). The program has systematically deployed ice-based buoys on the Arctic Sea ice in Arctic ocean, establishing a comprehensive observational grid for Arctic Sea ice buoys. The buoy positioning methods encompass both the Argos and GPS systems, rendering respective geographic accuracies of 300 and 100 m [43]. Leveraging the specified onset and termination timestamps, the average speed of the sea ice represented by the buoy is derived through the computation of its relative displacement. The IABP buoy data can be readily accessed online.[2]

D. Manually Reference Data

The processing steps for making the reference data are as follows. First, load the C-SAR/01 pairs imagery into the ArcGIS software and then project the images to the WGS 84/NSIDC Sea Ice Polar Stereographic North (EPSG:3413) coordinate system. Visually interpret and identify distinct corresponding points on the sea ice in both images, recording their respective x and y coordinates and calculate sea ice drift vectors (7) and (8). We control the difference between start points of image 1 and

image 2 to be within 10 km, ensuring the quality of the matched corresponding points.

III. METHODS

The procedure for sea ice drift extraction is included as follows.
1) SAR preprocessing.
2) Comparison of NRCS and PR features.
3) Sea ice drift vector extracting.
4) Removal of erroneous drift vectors.
5) Accuracy assessment.

A. SAR Preprocessing

1) C-SAR/01: The SAR is first radiometrically corrected, the original image is corrected to the backscatter coefficient and obtain the normalized radar cross section (NRCS) images for C-SAR/01 as follows:

$$\sigma_{C-SAR01} = 10\log_{10}\left(P^I * \left(\frac{\text{QualifyValue}}{65535}\right)^2\right) - K_{dB} \quad (1)$$

where $\sigma_{C-SAR01}$ is the backscattering values in the linear units for C-SAR/01 image, QualifyValue and K_{dB} are the quality value and calibration constant, and $P^I = DN^2$ is the magnitude of C-SAR/01 image, respectively.

Subsequently, multilooking processing and Lee filtering are applied. The spatial sampling window size was determined based on the radiation-corrected image to mitigate speckle noise, resulting in an average size of 7×7; in addition, traditional Lee filtering was performed on the multilooking images to further diminish the effects of speckle noise. Finally, based on its rational polynomial coefficient, the image was reprojected to WGS 84/NSIDC Sea Ice Polar Stereographic North (EPSG:3413) projection system with an encoded resolution of $250\,\text{m} \times 250\,\text{m}$ in x and y displacement.

---

[1][Online]. Available at: https://search.asf.alaska.edu/.
[2][Online]. Available at: https://iabp.apl.uw.edu/index.html.

2) Sentinel-1: Formula (2) was utilized for conducting radiometric calibration on the Sentinel-1 data

$$\sigma_{\text{Sentinel}-1} = \frac{\text{DN}^2}{A^2} \qquad (2)$$

where $\sigma_{\text{Sentinel}-1}$ is the backscattering values in the linear units for Sentinel-1 image, DN is the digital number provided in the TIFF file, and A is the value of the normalization coefficient from the accompanying calibration metadata.

The subsequent processing steps are the same as those for C-SAR/01, but during the projection, the georeferencing is based on the GDAL data model, where georeference information is stored as ground control points (GCPs). Originally, GCPs consisted of pairs of latitude/longitude and corresponding pixel/line coordinates.

B. Comparison of NRCS and PR Features

Sea ice drift vector research has focused on using NRCS, other different polarizations are ignored, such as polarization ratio (PR), polarization difference, and so on. The optimal sea ice change detection factors were screened, and the rapid identification mechanism of sea ice change detection factors was proposed. Research indicates that, in comparison with the analysis approach that utilizes SAR intensity imagery, the GLCM stands out as the optimal texture feature for these evaluations [44]. In this study, the relationship between NRCS and PR in the SAR images before and after the same sea ice target module was studied, and the rapid identification mechanism of sea ice change detection factors was proposed to find the optimal characteristics

$$\text{PR} = \frac{\text{NRCS}_{\text{HV}}}{\text{NRCS}_{\text{HH}}} \qquad (3)$$

where NRCS_{HV} means the NRCS for HV polarization, NRCS_{HH} means the NRCS for HH polarization.

To better understand NRCS and PR features how to get more sea ice drift vectors, Std GLCM information are used to measure the richness of grayscale information for two features. The GLCM, denoted $G(i, j)$, gives the co-occurrence probability between gray levels *i* and *j*, and is defined as

$$S(i, j) = \frac{G(i, j,)}{\sum_{i, j=1}^{K} G(i, j)}. \qquad (4)$$

And Std texture information can be calculated [45]

$$\text{Std} = \sqrt{\left(\sum_{i, j=1}^{K} G(i, j) * (i - \mu_x) \right)^2} \qquad (5)$$

where $G(i, j,)$ represents the number of occurrences of gray levels, i, j denote different pixels. And K and μ_x are the quantized number of gray levels and mean value of rows, respectively. In this study, the sliding window is 5×5, the statistical direction is over four directions (0°, 45°, 90°, 135°), the displacement is 1, and the gray level is 8.

C. Sea Ice Drift Vector Extraction

ORB is a feature-tracking algorithm developed by Rublee et al., improving upon the FAST keypoint detector and the binary

BRIEF descriptor by incorporating numerous modifications to enhance its overall performance [39].

1) Before the FT algorithm can be applied, the images have to be transformed into the intensity I range of 0 and 255. The transformation is done by using the following equation:

$$i = 255 * \frac{\sigma^0 - \sigma_{\min}^0}{\sigma_{\max}^0 - \sigma_{\min}^0} \qquad (6)$$

where $\sigma_{\min}^0$ and $\sigma_{\max}^0$ represent the 0.5th and 100th percentiles of σ^0, respectively. And when utilizing the NRCS image, $\sigma^0 = \text{NRCS}$, when using the PR image, $\sigma^0 = \text{PR}$.

2) The earlier image in the image pair is selected as the reference image (Image 1), whereas the later image is considered as the target image (Image 2). ORB feature operators are employed to extract feature points and matched using a brute-force matching method to obtain pairs of matching points. Please refer to [38] for the detailed procedures of ORB.

The nearest neighbor distance ratio (NNDR) test is commonly used in the FT algorithm to retain correct matching point pairs and filter out erroneous ones. The sea ice drift similarity of matching point pairs is measured by the matcher based on the Hamming distance between the feature point descriptors. By setting the threshold for NNDR test, matching point pairs with distance ratio values greater than the NNDR threshold were filtered out as erroneous matches. Empirically, when this distance ratio is below 0.8, around 90% of the matched points are incorrect [46]. However, it is challenging to use a fixed threshold for filtering out correct matching point pairs due to variations in different image characteristics.

3) After obtaining the matched point pairs, the geographical coordinates are obtained based on the image coordinates. Combined with the imaging time interval, the sea ice drift vectors can be derived for both *x* (7) and *y* (8) displacement. We calculate the sea ice drift velocity vectors by combining the retained matching point pairs with their geographical coordinates.

$$\nu_x = \frac{\Delta x}{\Delta t} \qquad (7)$$

$$\nu_y = \frac{\Delta y}{\Delta t} \qquad (8)$$

where ν_x and ν_y mean sea ice drift for *x* displacement and *y* displacement, Δt is the time interval between the two images, and $\Delta x = x_2 - x_1$ and $\Delta y = y_2 - y_1$ are sea ice drift for *x* and *y* displacement, respectively.

The maximum threshold for sea ice drift velocity is set to 50 cm/s, and any sea ice drift velocity vectors exceeding 50 cm/s are considered erroneous and subsequently removed.

D. Removal of Erroneous Sea Ice Drift Vectors

The FT algorithm has a higher computational efficiency compared to template matching. However, it tends to produce error-prone matching point pairs during the matching process, leading to erroneous sea ice drift vectors. Therefore, the error vector filtering method for sea ice drift based on FT algorithms

is continually being proposed and improved [47], [48], [49]. However, the focus should not be on error correction in sea ice drift results, but rather on targeted improvements to the sea ice drift inversion method to enhance the accuracy of sea ice drift inversion results.

Thus, based on the optimal feature SAR imagery, the FT method improves the sea ice drift extracted results by employing a local outlier factor (LOF) method to remove erroneous variables. The LOF algorithm first calculates the local reachability density of each data point and then compares this point's local reachability density with that of its neighboring points to derive the LOF for that point. This LOF indicates the degree of abnormality of the point relative to its neighboring points, with a larger value indicating a higher degree of abnormality. By computing the LOF for each data point, the LOF algorithm is able to identify data points with density abnormalities relative to their surrounding data points, thus recognizing outliers within the entire dataset. In this context, the number of neighboring points to consider for local reachability density is set to 160, which leads to more accurate density estimation.

E. Accuracy Assessment

The R^2, mean absolute error (MAE), error ratio, and root mean square error (RMSE) of the velocity are used as metrics of the accuracy of the algorithms.

1) For C-SAR/01, references for verifying the accuracy of automatically extracted sea ice drift vectors from each algorithm include manually extracted sea ice drift vectors (using FT in ArcGIS software) and buoy drift vectors. For sea ice drift vectors manually extracted, distance between the start point of the manually extracted vector and that of sea ice drift vector extracted from the C-SAR/01 images were the nearest possible and did not exceed 10 km [40]. This verification utilizes C-SAR/01 Pairs I and II to assess the accuracy of the algorithms.

In the case of IABP buoy data, the distance between the start point of IABP buoy data and that of the sea ice drift vector extracted from the C-SAR/01 images were the nearest possible and did not exceed 10 km. In addition, the time difference between the IABP starting point and starting point of the algorithm's automatically extracted vector from C-SAR/01 imagery should not exceed 15 min. This verification uses C-SAR/01 Pairs III to assess the accuracy of the algorithms with IABP buoy data.

2) For Sentinel-1, the start positions of the IABP buoy drift vectors and the vectors extracted from the Sentinel-1 images are different and must be matched. The nearest neighbor method was used for pairing. The distance between the start point of IABP buoy data and that of sea ice drift vector extracted from the Sentinel-1 images was the nearest possible and did not exceed 10 km. In addition, the time difference between the IABP starting point and starting point of the algorithm's automatically extracted vector from Sentinel-1 should not exceed 15 min.

IV. RESULTS

A. Find Optimal Parameter

The effectiveness of the number of retained keypoints on the sea ice drift vectors field depends on the selected threshold,
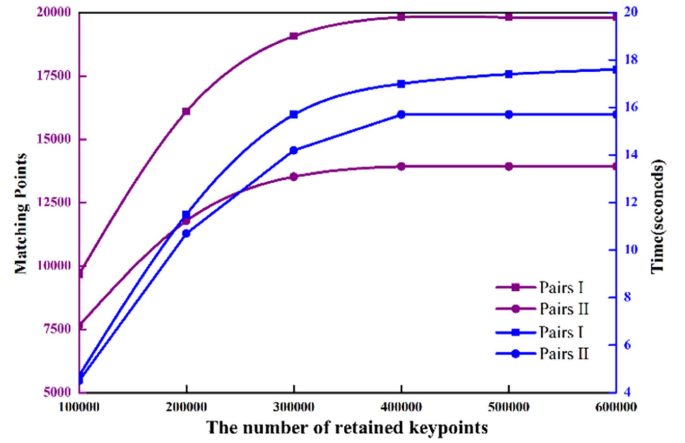

Fig. 2.   Effect of the number of retained keypoints of ORB on the expended time and total matching pairs for C-SAR/01 images acquired in TOPW mode.

which must be adjusted based on the acquired images. In order to better select a suitable threshold, the algorithm described in this article is used to extract sea ice drift velocity vectors for different number of maximum retained features, which is depicted in Fig. 2. However, the number of retained keypoints for the feature matching operator is mostly set to 100 000. Here, we set the number of retained keypoints for the ORB operator to be 100 000, 200 000, 300 000, 400 000, 500 000, and 600 000, respectively (see Fig. 2). It can be observed that the change trend of the two images is basically consistent. With the increase of the maximum retained keypoints, the time for feature matching and the number of matching keypoints pairs reach their maximum at 400 000. When the number of retained keypoints is 100 000, the extracted matching keypoints pairs are only half of the 400 000, while the time spent is only 11–13 s longer. It is due to the high computational efficiency of the ORB operator. When the number of retained keypoints is set to a value greater than 400 000, the number of matching pairs and the time spent are basically the same as when the number of retained keypoints is 400 000. At the number of retained keypoints of 400 000, the number of matching pairs and the matching time of sea ice drift were comparable to those at 300 000, with slightly more matching pairs at 400 000. Nevertheless, it remains uncertain whether the additional matching pairs represent correct or incorrect variables. Consequently, a further comparison of these two thresholds will be conducted to ascertain a more fitting the number of retained keypoints for the inversion of sea ice drift vectors.

Fig. 3. further demonstrates the impact of different numbers of retained keypoints (300 000 and 400 000) on the extraction of sea ice drift vectors. It can be observed that when the number of retained keypoints is 400 000, the inconsistent vector data noticeably increases, while the consistent vectors do not show a significant increase. This suggests that the additional matching point pairs in Fig. 2, compared to 300 000, may predominantly consist of inconsistent pairs. It seems that when the number of retained keypoints is set to 300 000, it is optimal for the ORB operator to extract sea ice drift vectors. Therefore, the number of retained keypoints for the algorithm described in this article is set to 300 000.
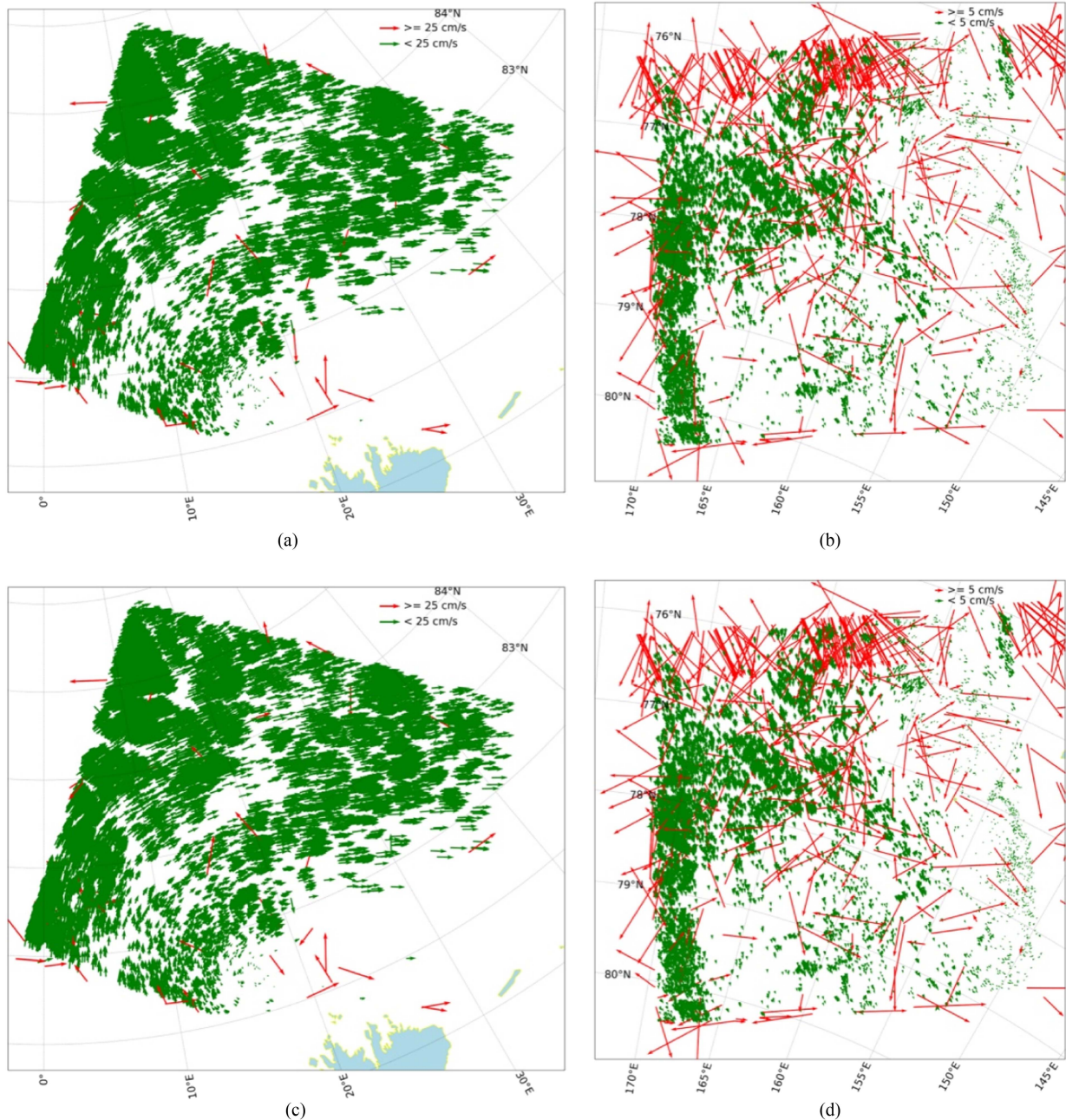
Fig. 3. Sea ice drift vectors derived with different features for C-SAR/01 images. The vectors derived from the Pairs I are shown as (a) 300 000; (c) 400 000; the vectors derived from the Pairs II are shown as (b) 300 000; (d) 400 000.

To select an appropriate NNDR ratio threshold, sea ice drift velocity vectors were extracted using different NNDR ratios based on C-SAR/01 image pairs. The results, as shown in Fig. 4 were evaluated using the number of matching pairs and the matching time of sea ice drift. It was observed that for NNDR ratios of 0.6, 0.7, 0.8, 0.9, and 1.0, both the number of matching points and the time of sea ice drift vectors from the sea ice drift vectors exhibited an increasing trend. While the highest number of image matching pairs were obtained at an NNDR ratio of 1.0 (Pairs I: 40 291, Pairs II: 63 960), the matching time of sea ice drift also reached its maximum (Pairs I: 14.8, Pairs II: 16.8), indicating the greatest data instability. This phenomenon is attributed to the inherent drawback of feature matching, which

tends to generate numerous erroneous matching pairs. Even with error variable filtration, a significant number of erroneous variables are retained. Conversely, at an NNDR ratio of 0.6, both the number of matching pairs and the matching time of sea ice drift reached their minimum. However, this reduction also led to the exclusion of a substantial number of accurate sea ice drift variables. At an NNDR ratio of 0.7, the number of matching pairs and the matching time of sea ice drift velocity were comparable to those at 0.8, with slightly more matching pairs at 0.8. Nevertheless, it remains uncertain whether the additional matching pairs represent correct or incorrect variables. Consequently, a further comparison of these three thresholds (NNDR of 0.7, 0.75, and 0.8) will be conducted to ascertain a
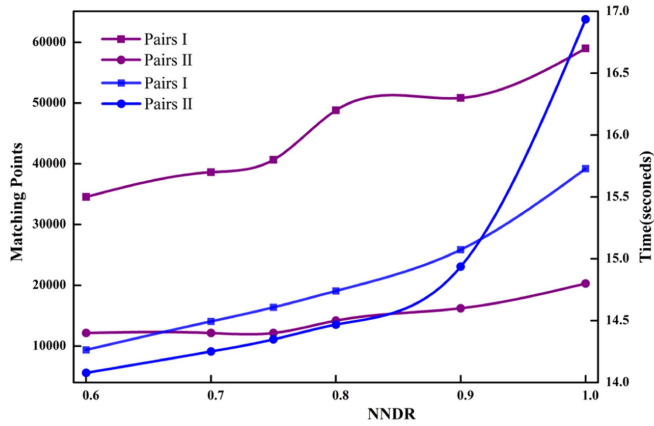
Fig. 4. Effect of the NNDR ratio on the expended time and total matching Points for HV-polarized C-SAR/01 images acquired in TOPW mode.

more fitting NNDR ratio value for the inversion of sea ice drift vectors.

Fig. 5 further demonstrates the influence of different NNDRs on the extraction of sea ice drift. Initially, for SAR Pairs I and Pairs II imagery, as NNDR increases, the number of inconsistent sea ice drift vectors gradually rises, peaking when NNDR reaches 0.8. In the case of Pairs I, the increase in NNDR leads to a relatively smaller growth in inconsistent sea ice drift vectors. However, for Pairs II, there is a significant increase in the number of sea ice drift vectors as NNDR increases. This may be attributed to the limitation imposed by setting the number of retained keypoints to 30 000, while the correct sea ice drift quantity for Pairs II is relatively low. Pairs I and Pairs II represent two scenarios of sea ice drift vector extraction. Pairs I signifies a situation where the correct sea ice drift vector data is consistent with the maximum retention quantity, whereas Pairs II represents a scenario where there is a significant disparity between the correct sea ice drift vectors and the maximum retention quantity. In both cases, when NNDR equals 0.75, it better preserves the correct sea ice drift vectors and also helps in removing some incorrect vectors, laying a solid foundation for filtering out erroneous sea ice drift vectors in subsequent steps. Therefore, the NNDR for the algorithm described in this article is set to 0.75. The number of retained keypoints of 300 000 and NNDR of 0.75 were used to sea ice drift vectors extracting for the following study.

B. Comparison of the Result Yielded With Two Features

Based on the mentioned findings, this study opted to extract sea ice drift vectors from C-SAR/01 images at a resolution of 250 m under the TOPW mode, setting the number of retained keypoints at 300 000 and NNDR at 0.75. Fig. 6 presents the distribution of sea ice drift vectors obtained by matching different features (NRCS and PR) from two pairs of image pairs. While the patterns of drift vectors are highly sea ice drift similar at corresponding locations between the two sets of image pairs, the extracted data volume of drift vectors exhibits significant discrepancies. The sorting of data points obtained from the two sets of image pairs reveals that NRCS yields a greater data

volume than PR. Examining the sea ice drift vector fields from the two sets of image pairs, all two feature types demonstrate notable similarities in both magnitude and direction. However, the NRCS inversion yields a greater number of sea ice drift vectors. This may be related to the richness of the GLCM information for each feature.

All sea ice drift vector results underwent testing using the algorithm proposed in this article. Table II provides the feature point counts and sea ice drift vectors obtained after sea ice drift vectors extraction from different features. Significant differences exist in the number of feature points extracted by different feature matching operators in the images. In both Pairs I and Pairs II, NRCS generate more feature points comparing to PR features imagery, consequently resulting in more drift vectors. The consistent spatial distribution of these feature points indicates that the number of extracted feature points determines the spatial distribution of the sea ice drift velocity vector field. Therefore, to achieve a more uniform distribution of sea ice drift vector fields in subsequent analyses, it may be necessary to enhance the image features.

Fig. 7 displays the Std GLCM information extracted from the NRCS image and the PR image over four directions (0°, 45°, 90°, 135°). The results indicate that the Std GLCM information extracted from the PR image is higher than the NRCS image with pairs I and pairs II over four directions, which indicates the direction does not influence obtaining the number of feature points. With the increase of the Std GLCM, the number of feature point pairs is relatively low (see Table II). This may be due to the fact that STD represents the variation in image grayscale. When STD is large, the grayscale variation in the image is large, and the feature points are concentrated in the pixels with large grayscale variation. However, the grayscale variation over sea ice is not large, thus neglecting many detailed feature points. For the NRCS image, the relationship between Std GLCM and the number of feature points is not entirely inverse. This may be due to the fact that the PR feature represents the dielectric coefficient, which reflects large-scale sea ice information more effectively, while the NRCS feature represents sea surface roughness, which is more indicative of small-scale sea ice information.

C. Results of Sea Ice Drift Vectors Filtering

The NNDR test relies on the correlation properties between the descriptors of the feature points, which are unrelated to the characteristics of sea ice drift. Therefore, the results of the NNDR test will still retain a certain number of erroneous vectors, as can also be observed from Fig. 6. Therefore, this article proposes the LOF method to remove erroneous sea ice drift vectors. To be compared, Fig. 8 illustrates the results of the common Confidence interval algorithm and LOF algorithm in filtering using Pairs I and Pairs II C-SAR/01 NRCS imagery. The sea ice drift vector extracted method proposed integrates a supplementary filtering algorithm based on Confidence interval algorithms and LOF algorithm, respectively. It is observed that in both Pairs I and Pairs II, the confidence interval method can remove right vectors with Confidence interval algorithms [see Fig. 8(a)], meanwhile, erroneous vectors still persist Confidence
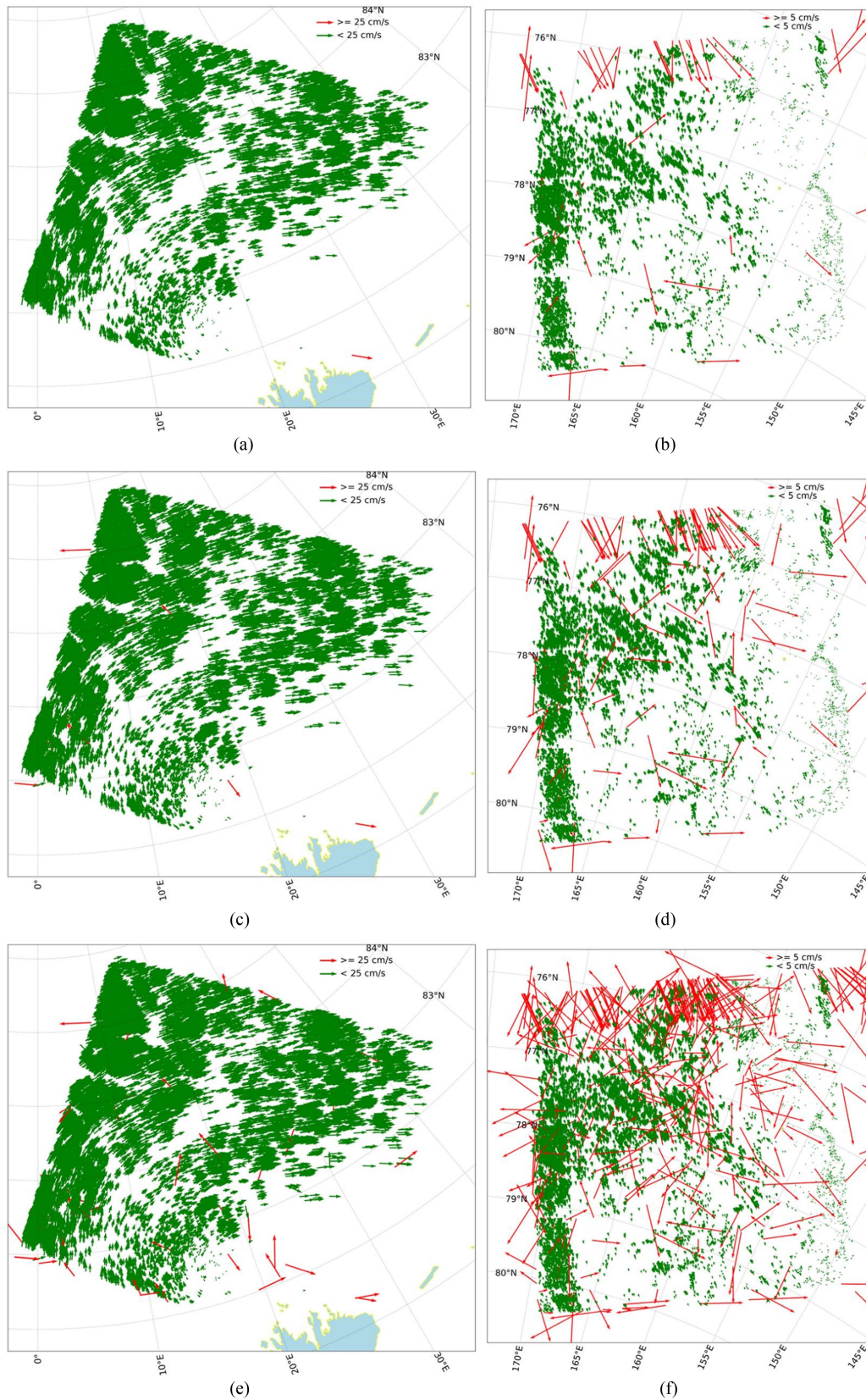
Fig. 5. Sea ice drift vectors derived with different Features for C-SAR/01 images. The vectors derived from the Pairs I are shown as (a) 0.7; (c) 0.75; (e) 0.8. The vectors derived from the Pairs II are shown as (b) 0.7; (d) 0.75; (f) 0.8.
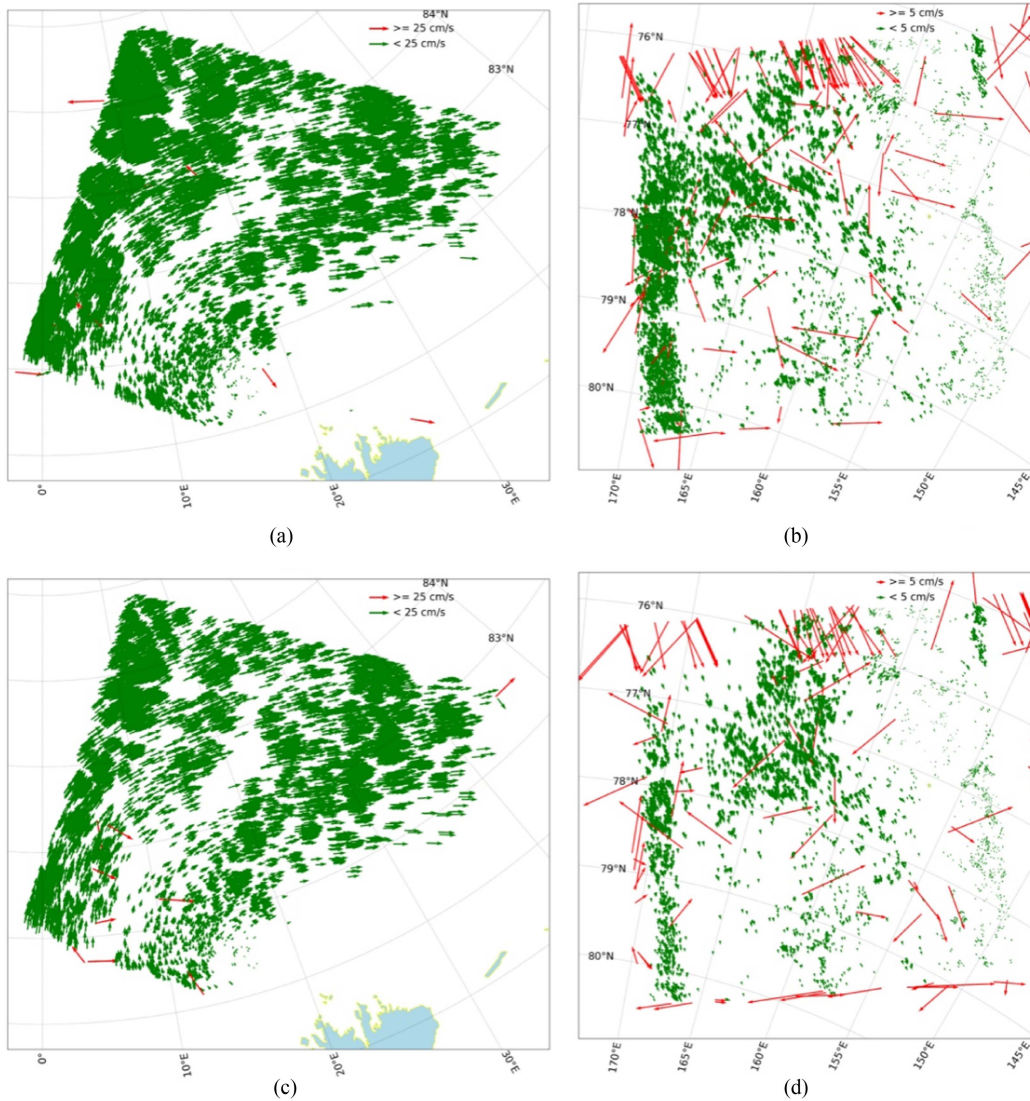
Fig. 6. Sea ice drift vectors derived with different features for C-SAR/01 images with NNDR of 0.7. The vectors derived from the Pairs I are shown as (a) NRCS; (c) PR; the vectors derived from the Pairs II are shown as (b) NRCS; (d) PR.

TABLE II
MATCHING RESULTS OF DIFFERENT FEATURES

Satellite	No.	Feature	Number of feature points in the image 1	Number of feature points in the image 2	Matching points
C-SAR/01	Pairs I	NRCS	152513	182957	16386
		PR	126646	181931	11200
C-SAR/01	Pairs II	NRCS	139614	183979	11094
		PR	127836	164548	5569

interval algorithms [see Fig. 8(b)]. Because the distribution of these sea ice drift vectors does not strictly follow a total normal distribution, thus making it ineffective in computing confidence intervals and selecting the correct vectors. However, the LOF algorithm establishes a model for determining outliers, thereby avoiding the removal of correct sea ice drift vectors.

The LOF algorithm effectively retains a significant number of correct sea ice drift vectors while eliminating erroneous ones.

Fig. 9 illustrates the component distribution histograms after Confidence interval and LOF algorithms filtering for Pair I imagery as an example, separated into the x and y directions.
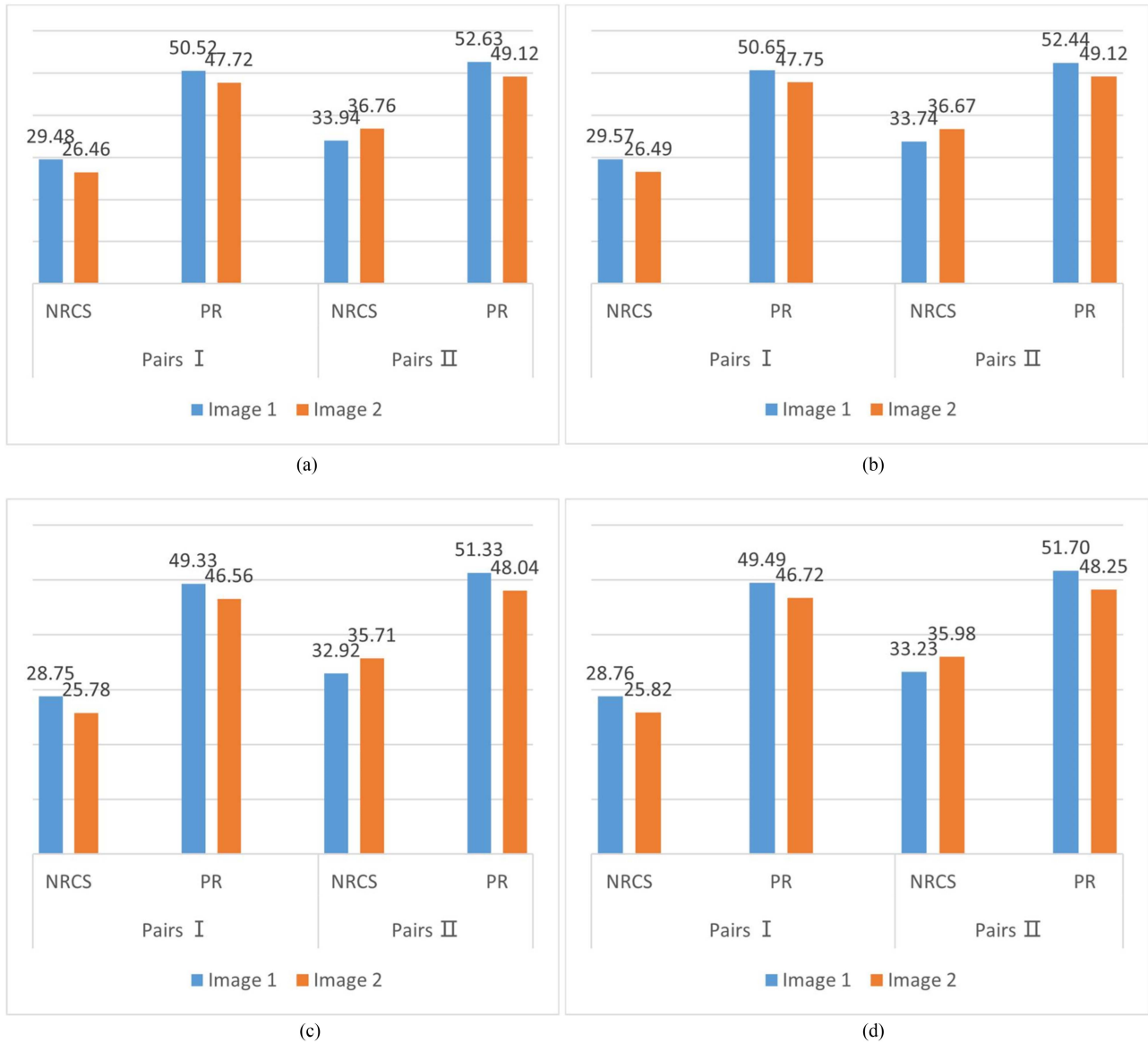
Fig. 7. Std GLCM information from C-SAR/01 images. (a) Direction=0°. (b) Direction=45°. (c) Direction=90°. (d) Direction=135°.

When filtering with Confidence interval algorithm, this step has already retained a large number of extreme big erroneous values, which further disperses the data, thereby exacerbating the difficulty of confidence interval filtering. However, the LOF algorithm can remove most of the unusually large values, which makes the x and y component distribution in accordance with the value of confidence interval distribution. In conclusion, the LOF algorithm proposed in this study leverages the feature distribution of vector components, enabling effective computation of confidence intervals and selection of the correct vectors.

From the above-mentioned analysis, it can be concluded that it is feasible to extract sea ice drift vectors using the ORB FT algorithm with C-SAR/01 SAR NRCS imagery. Specifically, setting NNDR to 0.75, the maximum retainable quantity to 300 000, and utilizing the LOF algorithm for filtering. In order to further authenticate the robustness of sea ice drift vectors

extracted from SAR data presented in this article, experiments were carried out to compare the precision of sea ice drift vector speed and direction obtained from Sentinel-1 SAR images. The results are depicted in Fig. 10, it can be observed that the use of the confidence interval exclusion algorithm leads to a noticeable gap in the top-right corner [see Fig. 10(a)] and the lower-left corner [see Fig. 10(b)] of the image, which is attributed to the nonconformity of the vector component distribution to a normal distribution. Despite the minimal rotation in the drift field, the confidence interval algorithm erroneously filters out the edges. The algorithm proposed in this article utilizes the LOF algorithm to effectively retain the correct drift vectors while removing erroneous ones, significantly improving accuracy. This demonstrates the accuracy and robustness of the LOF algorithm proposed in this article for extracting sea ice drift vectors from SAR data again.
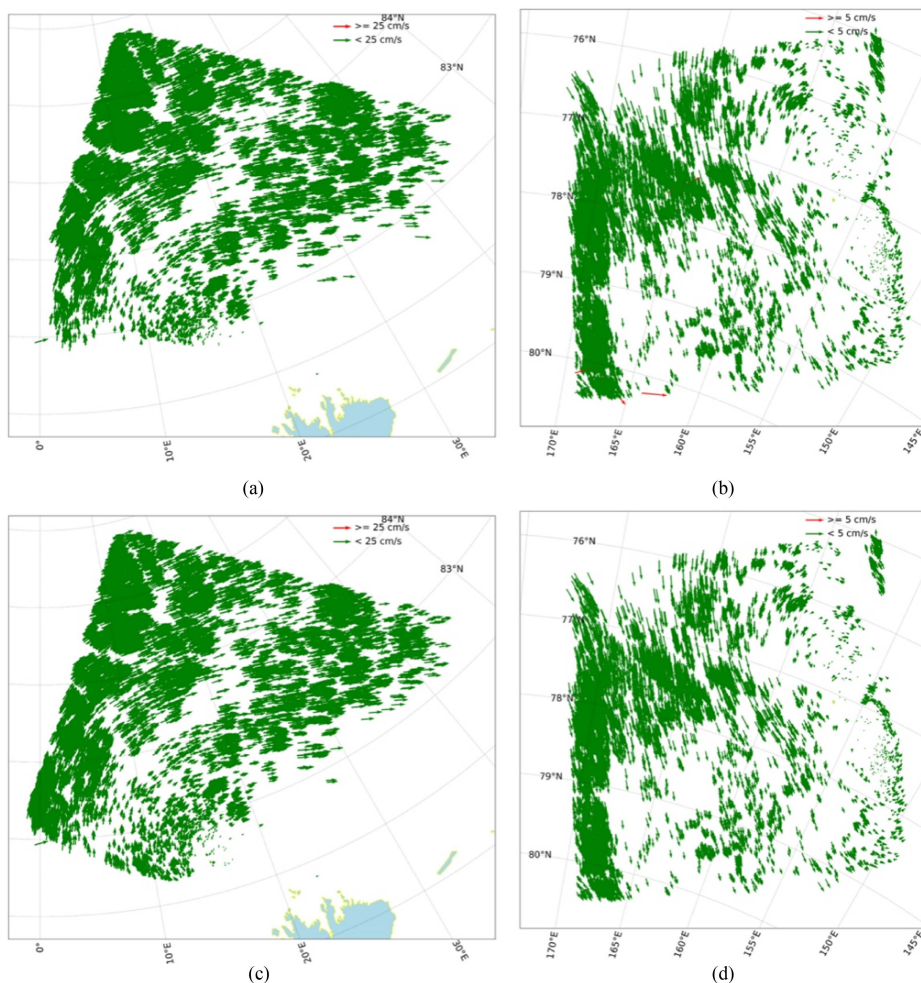
Fig. 8. Sea ice drift vectors derived for C-SAR/01 Pairs I images. (a) Confidence interval filtering. (c) LOF algorithm; sea ice drift vectors derived for C-SAR/01 Pairs II images. (b) Confidence interval filtering. (d) LOF algorithm.
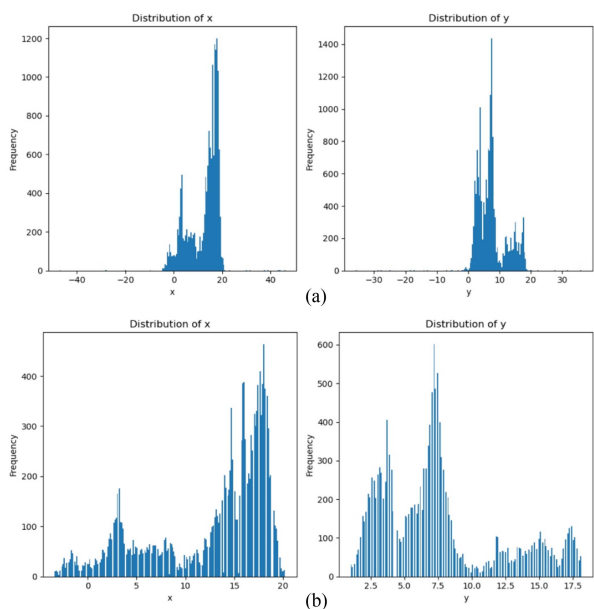

Fig. 9. Histograms of x and y components of sea ice drift vectors for Pairs I. (a) Confidence interval algorithms. (b) LOF algorithm.

D. Accuracy and Effectiveness

The accuracy of the extracted sea ice drift vectors was assessed by the method described in Section III-E using sea ice drift data manually extracted from C-SAR/01 images and IABP buoy data. We did not directly assess the sea ice drift vectors extracted from C-SAR/01 imagery using currently released sea ice drift products because the temporal resolution of these products does not match that of the sea ice drift data extracted from C-SAR/01. In addition, we selected the IABP buoy extracted from SAR images to assess the sea ice drift vectors extracted from Sentinel-1 images to ensure their reliability as reference data.

1) This study assesses the precision of sea ice drift vector speed and direction derived from C-SAR/01 SAR Pairs I and Pairs II imagery, comparing them with reference data manually extracted. Fig. 11 illustrates the findings, showing a substantial level of concordance between the proposed method and the reference buoy, which the R^2 of speed value and direction are 0.980 and 0.998, respectively. In addition, the comparison between the sea ice drift results extracted from the C-SAR/01 SAR imagery (Pairs III) and the IABP buoy data for ID of 900 128 yields
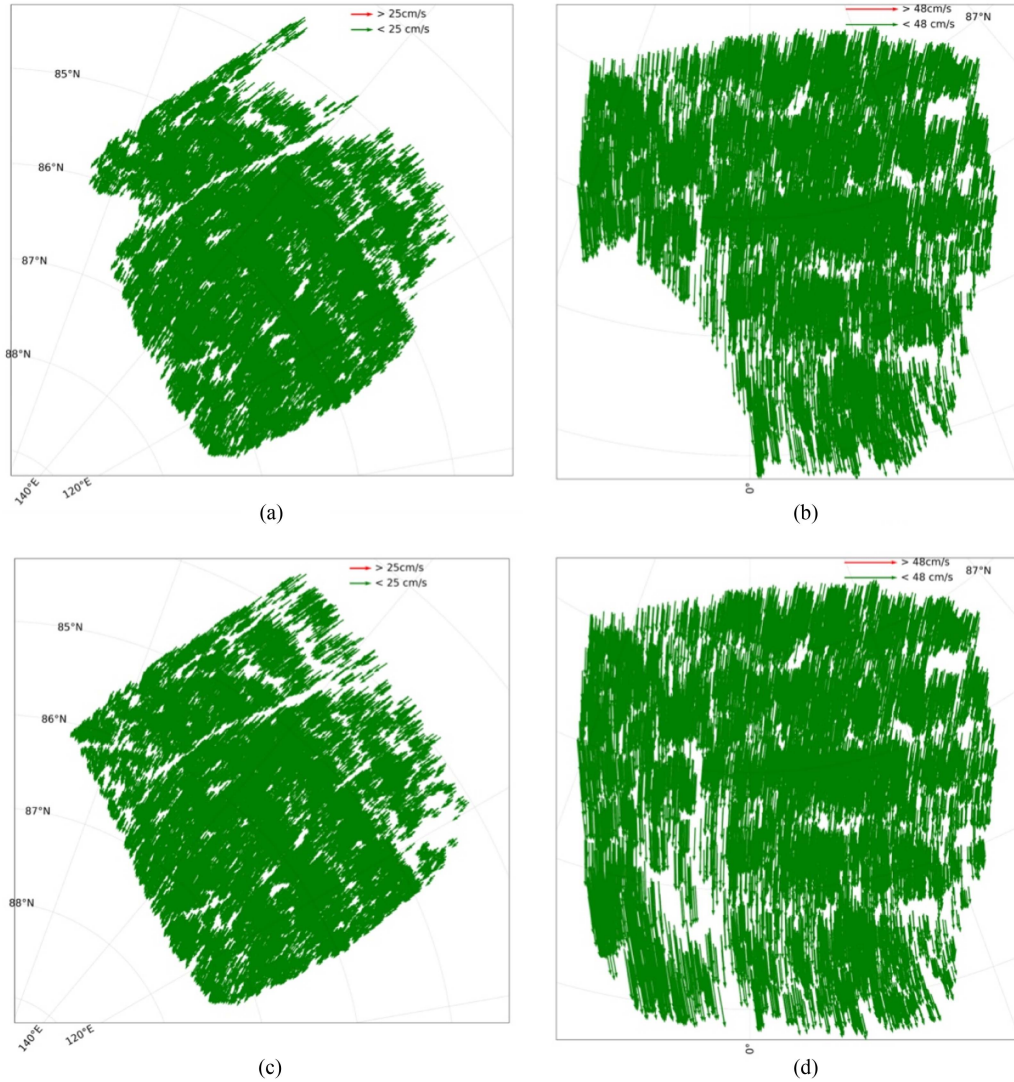
Fig. 10. Sea ice drift vectors derived for Sentinel-1 with Pairs IV images. (a) Confidence interval method. (c) LOF algorithm; sea ice drift vectors derived for Sentinel-1 with Pairs V images. (b) Confidence interval method. (d) LOF algorithm.
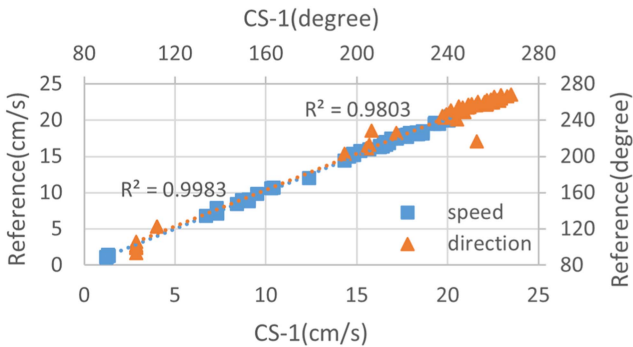

Fig. 11. Sea ice drift vectors derived from C-SAR/01 validation to manually extracted reference data.

respective sea ice drift speeds of 0.76 and 0.49, with directions of 283.4° and 299.4°. The differences in speed and direction are 0.27 and 16°, respectively. It indicates strong coherence between the sea ice drift vectors extracted via

improvement of ORB feature matching algorithms in this study.

2) In order to further authenticate the robustness of the sea ice drift velocity field extracted from Sentinel-1 SAR data presented in this article, experiments were carried out to compare the precision of sea ice drift vector speed and direction obtained from Sentinel-1 SAR Pairs IV and Pairs V imagery with reference data derived from IABP buoy records. The results are depicted in Fig. 12 with the R^2 of speed and direction are 0.913 and 0.942, respectively, exhibit a significant level of agreement between the proposed method and the IABP buoy data. In conclusion, with the R^2 higher than 0.9, it further authenticates the robustness of sea ice drift velocity field extracted from SAR data presented in this article.

In Table III, detailed accuracy information is provided in terms of the speed and direction of the sea ice drift vector distribution extracted from the CSAR/01 and Sentinel-1 SAR data corresponding to Figs. 11 and 12. In the case of C-SAR/01,

TABLE III
VALIDATION RESULTS OF DIFFERENT SAR DATA IN SPEED AND DIRECTION

Satellite	Velocity	N	R^2	RMSE	MAE	Error Ratio
C-SAR/01	Speed(cm/s)	54	0.998	0.273	0.226	3.12%
	Direction(°)		0.980	7.794	5.332	2.61%
Sentinel-1	Speed(cm/s)	157	0.913	1.339	1.180	7.91%
	Direction(°)		0.942	3.921	2.208	1.11%
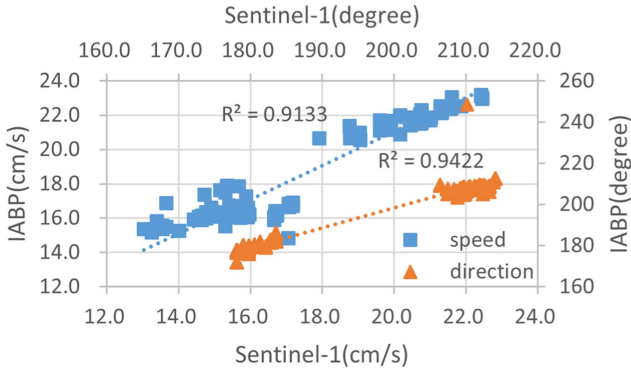
Fig. 12. Sea ice drift vectors derived from Sentinel-1 validation to IABP buoy data.

the RMSE for speed and direction stands at approximately 0.273 cm/s and 7.794°, respectively. Meanwhile, the MAE for speed and direction resides at approximately 0.226 cm/s and 5.332°, respectively. Notably, the error ratio for both speed and direction are 3.12% and 2.61%. This suggests a high level of reliability in extracting sea ice drift vectors using the SAR NRCS imagery within the C-SAR/01 TOPW mode. In the case of Sentinel-1, the RMSE of speed and direction is approximately 1.339 cm/s and 3.921°; While the MAE of speed and direction is approximately 1.180 cm/s and 2.208°; the error ratio of speed and direction is approximately 7.91% and 1.10%. This also implies a substantial degree of dependability in the derivation of sea ice drift vectors through the utilization of SAR NRCS imagery within the Sentinel-1 EW mode. Generally, it is clear that the algorithm demonstrates universality for two different satellite SAR data, thereby proving the effective applicability of this method for sea ice drift vector extracting.

V. CONCLUSION

This article presents the process of extracting sea ice drift vectors from C-SAR/01 images using the improved ORB FT algorithm. The comparison of the retained keypoints number and NNDR on the extraction of sea ice drift vectors using the ORB FT algorithm is discussed. In addition, the differences in the results and efficiency of sea ice drift vector extraction from C-SAR/01 images using the NRCS and PR features are compared and obtain the optimal features. Furthermore, the accuracy of extracted sea ice drift vectors from C-SAR/01 images is evaluated. The study applies the LOF algorithm to effectively eliminate incorrectly extracted sea ice drift vectors while retaining the correct vectors, thereby enhancing the removal of erroneously extracted sea ice drift vectors by an improved ORB FT algorithm.

1) By comparing the time taken to obtain sea ice drift vectors from C-SAR/01 images with different retained keypoints numbers, it was observed that as the number of retained keypoints increased, the number of feature matching point pairs reached its peak at 300 000. Thus, when the number of retained keypoints was set to 300 000, it was considered to be the best value for extracting sea ice drift vectors using the ORB operator. The NNDR also influences the reliability of extracted sea ice drift vectors. an NNDR of 0.75 resulted in the extraction of a high-density sea ice drift vector field, while simultaneously removing a significant number of erroneous vectors. In addition, this article proposes an LOF algorithm, which can effectively assist in identifying and removing erroneous values within the sea ice drift vectors.

2) The study compared the effectiveness of two commonly used features, NRCS and PR, in extracting sea ice drift vectors from C-SAR/01 TOPW mode imagery. From the sea ice drift vector extracted from image pairs, two features exhibited significant similarities in terms of speed and direction. The NRCS image provided a more densely distributed sea ice drift vector. The number of sea ice drift vectors extracted from the NRCS imagery was comparable to that from the PR imagery; however, the NRCS image produced almost twice the number of matching point pairs as the PR image.

3) The accuracy of extracted sea ice drift vectors from C-SAR/01 images were evaluated using manually extracted sea ice drift vectors as reference data. The study also used IABP buoy data to evaluate the extracted sea ice drift vectors from Sentinel-1 images. The R^2 and error ratio of speed value and direction are over 0.90 and lower than 8%. This indicates the accuracy and reliability of the algorithm that sea ice drift vector fields extracted from different SAR satellite imagery in this article.

In conclusion, the analysis mentioned above mainly illustrates that by utilizing C-SAR/01 images, along with the improved ORB FT method, and by conducting appropriate erroneous matching removal, it is possible to efficiently and rapidly generate high-resolution Arctic Sea ice drift fields. With the expansion of C-SAR/01 satellite coverage in the Arctic region, future research will utilize C-SAR/01 satellite images in more areas for sea ice drift vectors studies, providing precise and detailed

data support for environmental and climate studies in the Arctic region and offering data services for Arctic shipping safety.

REFERENCES

[1] T. A. Moon et al., "Arctic Report Card 2022: Greenland Ice Sheet," 2022, doi: 10.25923/c430-hb50.

[2] G. Spreen, L. Steur, D. Divine, S. Gerland, E. Hansen, and R. Kwok, "Arctic sea ice volume export through Fram Strait from 1992 to 2014," *J. Geophys. Res. Ocean.*, vol. 125, no. 6, 2020, Art. no. e2019JC016039, doi: 10.1029/2019JC016039.

[3] L. H. Smedsrud, M. H. Halvorsen, J. C. Stroeve, R. Zhang, and K. Kloster, "Fram Strait sea ice export variability and September Arctic sea ice extent over the last 80 years," *Cryosphere*, vol. 11, no. 1, pp. 65–79, 2017, doi: 10.5194/tc-11-65-2017.

[4] A. I. Felzenbaum, "The theory of steady drift of ice and the calculation of the long period mean drift in the central part of the Arctic Basin," *Probl. Severa*, vol. 2, pp. 16–46, 1958.

[5] P. Fan et al., "Sea ice surface temperature retrieval from Landsat 8/TIRS: Evaluation of five methods against in situ temperature records and MODIS IST in Arctic region," *Remote Sens. Environ.*, vol. 248, 2003, Art. no. 111975, doi: 10.1016/j.rse.2020.111975.

[6] J. Su, H. D.Wu, M. A. Knuth, and G. P. Gao, "Modeling dynamic interaction of ice-Ocean in the Bohai Sea," *J. Glaciol. Geocryol.*, vol. 25, pp. 292–298, 2020, doi: 10.3969/j.issn.1000-0240.2003.z2.018.

[7] X. Wang et al., "Assessing CMIP6 simulations of Arctic Sea ice drift: Role of near-surface wind and surface ocean current in model performance," *Adv. Clim. Change Res.*, vol. 14, no. 5, pp. 691–706, 2023, doi: 10.1016/j.accre.2023.09.005.

[8] J. V. Lukovich, D. G. Babb, and D. G. Barber, "On the scaling laws derived from ice beacon trajectories in the southern Beaufort Sea during the International Polar Year-Circumpolar Flaw Lead study, 2007-2008," *J. Geophys. Res. Oceans*, vol. 116, no. C9, 2011, doi: 10.1029/2011JC007049.

[9] T. Lavergne, S. Eastwood, Z. Teffah, H. Schyberg, and L. A. Breivik, "Sea ice motion from low-resolution satellite sensors: An alternative method and its validation in the Arctic," *J. Geophys. Res. Oceans*, vol. 115, 2010, doi: 10.1029/2009JC005958.

[10] R. A. Hagen, M. F. Peters, R. T. Liang, D. G. Ball, and J. M. Brozena, "Measuring Arctic sea ice motion in real time with photogrammetry," *IEEE Geosci. Remote. Sens. Lett.*, vol. 11, pp. 1956–1960, Nov. 2014, doi: 10.1109/LGRS.2014.2314958.

[11] Y. X. Wang, Y. F. Liu, H. Guo, T. Y. Liu, and Y. S. Yang, "Research of image matching method in sea ice observation," *Comput. Eng. Appl.*, vol. 46, pp. 245–248, 2010, doi: 10.3778/j.issn.1002-8331.2010.35.071.

[12] R. Kwok, "Summer sea ice motion from the 18 GHz channel of AMSR-E and the exchange of sea ice between the Pacific and Atlantic sectors," *Geophys. Res. Lett.*, vol. 35, pp. 1–6, 2008, doi: 10.1029/2007GL032692.

[13] L. Y. Wang, Y. J. He, B. Zhang, and B. C. Liu, "Retrieval of Arctic sea ice drift using HY-2 Satellite scanning microwave radiometer data," *Haiyang Xuebao*, vol. 39, pp. 110–120, 2017, doi: 10.3969/j.issn.0253-4193.2017.09.011.

[14] Z. I. Petrou and Y. L. Tian, "High-resolution sea ice motion estimation with optical flow using satellite spectroradiometer data," *IEEE Trans. Geosci. Remote Sens.*, vol. 55, pp. 1339–1350, Mar. 2017, doi: 10.1109/TGRS.2016.2622714.

[15] Y. Fang, X. Wang, G. Li, Z. Q. Chen, F. M. Hui, and X. Cheng, "Arctic sea ice drift fields extraction based on feature tracking to MODIS imagery," *Int. J. Appl. Earth Observ.*, vol. 120, no. 103353, 2023, Art. no. 103353, doi: 10.1016/J.JAG.2023.103353.

[16] R. M. Ninnis, W. J. Emery, and M. J. Collins, "Automated extraction of pack ice motion from advanced very high resolution radiometer imagery," *J. Geophys. Res. Oceans*, vol. 91, no. 10725, pp. 10725–10734, 1986, doi: 10.1029/JC091iC09p10725.

[17] R. F. Wang, D. Huang, X. Zhang, and P. Wei, "Combined pattern matching and feature tracking for Bohai sea ice drift detection using Gaofen-4 imagery," *Int. J. Remote Sens.*, vol. 41, pp. 7486–7508, 2020, doi: 10.1080/01431161.2020.1760396.

[18] X. Zhang, Y. X. Zhu, J. Zhang, J. M. Meng, X. N. Li, and X. X. Li, "An algorithm for sea ice drift retrieval based on trend of ice drift constraints from Sentinel-1 SAR data," *J. Coastal Res.*, vol. 102, pp. 113–126, 2020, doi: 10.2112/SI102-015.1.

[19] A. S. Komarov and D. G. Barber, "Sea ice motion tracking from sequential dual-polarization RADARSAT-2 images," *IEEE Trans. Geosci. Remote Sens.*, vol. 52, pp. 121–136, Jan. 2014, doi: 10.2112/SI102-015.1.

[20] J. Karvonen, "Operational SAR-based sea ice drift monitoring over the Baltic Sea," *Ocean Sci.*, vol. 8, pp. 473–483, 2012, doi: 10.5194/os-8-473-2012.

[21] R. Kwok, V. Curlander, R. McConnell, and S. S. Pang, "An ice-motion tracking system at the Alaska SAR facility," *IEEE J. Ocean. Eng.*, vol. 15, no. 1, pp. 44–54, Jan. 1990, doi: 10.1109/48.46835.

[22] Y. J. Qiu and X. M. Li, "Retrieval of sea ice drift from the Central Arctic to the Fram Strait based on sequential sentinel-1 SAR data," *IEEE Trans. Geosci, Remote Sens.*, vol. 60, Dec. 2022, Art. no. 4306914, doi: 10.1109/TGRS.2022.3226223.

[23] S. E. L. Howell, M. Brady, and A. S. Komarov, "Generating large-scale sea ice motion from Sentinel-1 and the RADARSAT Constellation mission using the environment and Climate Change Canada automated sea ice tracking system," *Cryosphere*, vol. 6, pp. 1125–1139, 2022, doi: 10.5194/tc-16-1125-2022.

[24] X. Wang et al., "An improvement in accuracy and spatial resolution of the pattern-matching sea ice drift from SAR imagery," *Int. J. Dig. Earth*, vol. 16, no. 2, pp. 4073–4094, 2023, doi: 10.1080/17538947.2023.2264918.

[25] X. Wang, R. T. Chen, C. Li, Z. Q. Chen, F. M. Hui, and X. Cheng, "An intercomparison of satellite derived Arctic sea ice motion products," *Remote Sens.*, vol. 14, 2022, Art. no. 1261, doi: 10.3390/rs14051261.

[26] Q. Shi and J. Su, "Assessment of Arctic remote sensing ice motion products based on ice drift buoys," *J. Remote Sens. (Chin.)*, vol. 24, pp. 867–882, 2020, doi: 10.11834/jrs.20209038.

[27] S. Muckenhuber, A. A. Korosov, and S. Sandven, "Open-source feature-tracking algorithm for sea ice drift retrieval from Sentinel-1 SAR imagery," *Cryosphere*, vol. 10, pp. 913–925, 2016, doi: 10.5194/tc-10-913-2016.

[28] A. Komarov and D. Barber, "Detection of sea ice motion from Co- and cross-polarization RADARSAT-2 images," in *Proc. IEEE Int. Geosci. Remote Sens. Symp.*, 2012, pp. 3277–3280, doi: 10.1109/Igarss.2012.6350604.

[29] A. A. Korosov and P. A. Rampal, "Combination of feature tracking and pattern matching with optimal parametrization for sea ice drift retrieval from SAR data," *Remote Sens.*, vol. 9, 2017, Art. no. 258, doi: 10.3390/rs9030258.

[30] L. Li, Y. T. Zhu, J. Hong, F. Ming, and Y. Wang, "Design and implementation of a novel polarimetric active radar calibrator for Gaofen-3 SAR," *Sensors*, vol. 18, pp. 1–12, 2018, doi: 10.3390/s18082620.

[31] H. Wang et al., "Calibration of the copolarized backscattering measurements from Gaofen-3 synthetic aperture radar wave mode imagery," *IEEE J. Sel. Topics Appl. Earth Observ. Remote Sens.*, vol. 12, pp. 1748–1762, Jun. 2019, doi: 10.1109/JSTARS.2019.2911922.

[32] M. C. Li, C. X. Zhou, B. Li, X. L. Chen, J. Q. Liu, and T. Zeng, "Application of the combined feature tracking and maximum cross-correlation algorithm to the extraction of sea ice motion data from GF-3 imagery," *IEEE J. Sel. Top. Appl. Earth Observ. Remote Sens.*, vol. 15, pp. 3390–3402, Apr. 2022, doi: 10.1109/JSTARS.2022.3166897.

[33] T. Lavergne, S. Eastwood, Z. Teffah, H. Schyberg, and L. A. Breivik, "Sea ice motion from low-resolution satellite sensors: An alternative method and its validation in the Arctic," *J. Geophys. Res. Oceans*, vol. 115, pp. 1–14, 2010, doi: 10.1029/2009JC005958.

[34] F. Girard-Ardhuin, R. Ezraty, D. Croizé-Fillon, and J. Piolle, "Sea Ice Drift in the Central Arctic combining QuikSCAT and SSM/I Sea Ice Drift data. User's Manual, version 3.0, French Research Institute for the Exploitation of the Seas (Ifremer)," 2008. [Online]. Available: ftp://ftp.ifremer.fr/ifremer/cersat/products/gridded/psi-drift/documentation/merged.pdf

[35] T. Lavergne, Low Resolution Sea Ice Drift. Product User's Manual; Version 1.8; The Ocean and Sea Ice Satellite Application Facility (OSI SAF) 2016. [Online]. Available: https://osisaf-hl.met.no/sites/osisaf-hl.met.no/files/user_manuals/osisaf_cdop2_ss2_pum_sea-ice-drift-lr_v1p8.pdf

[36] M. Tschudi, W. N. Meier, J. S. Stewart, C. Fowler, and J. Maslanik, Polar Pathfinder Daily 25 km EASE-Grid Sea Ice Motion Vectors; Version 4. [The Arctic Region]; NASA National Snow and Ice Data Center Distributed Active Archive Center, Boulder, CO, USA, 2019. doi: 10.5067/IN-AWUWO7QH7B.

[37] R. Saldo and B. Hackett, Product User Manual for Global High Resolution SAR Sea Ice Drift SEAICE_GLO_SEAICE_L4_-NRT_OBSERVATIONS_011_006; Issue 2.12, Space Department/Institute at the Technical University of Denmark (DTU Space), 2020. [Online]. Available: https://catalogue.marine.copernicus.eu/documents/PUM/CMEMS-SI-PUM-011-006.pdf

[38] J. K. Wang, "Research on sea ice drift detection technology based on combination of feature tracking and pattern matching," M.S. thesis, Inner Mongolia Univ. Sci. Technol., Inner Mongolia, 2019, doi: 10.27724/d.cnki.gnmgk.2019.000187.

[39] E. Rublee, V. Rabaud, K. Konolige, and G. Bradski, "ORB: An efficient alternative to SIFT or SURF," in *Proc. Int. Conf. Comput. Vis.*, 2011, pp. 2564–2257, doi: 10.1109/iccv.2011.6126544.

[40] C. Y. Li, G. LI, X. Wang, Q. Ju, and Z. Q. Chen, "Sea ice drift vectors extraction based on feature tracking to Sentinel-1 images," *Nat. Remote Sens. Bull.*, pp. 1–10, 2022, doi: 10.11834/jrs.20222238.

[41] M. C. Li, C. X. Zhou, X. L. Chen, Y. Liu, B. Li, and T. Liu, "Improvement of the feature tracking and patter matching algorithm for sea ice motion retrieval from SAR and optical imagery," *Int. J. Appl. Earth. Observ.*, vol. 112, 2022, Art. no. 102908, doi: 10.1016/j.jag.2022.102908.

[42] Q. Q. Huang et al., "Quick quality assessment and radiometric calibration of C-SAR/01 satellite using flexible automatic corner reflector," *Remote Sens.*, vol. 15, no. 104, 2023, Art. no. 104, doi: 10.3390/rs15010104.

[43] D. Thomas, "The quality of sea ice velocity estimates," *J. Geophys. Res. Oceans.*, vol. 104, no. C6, pp. 13627–13652, 1999, doi: 10.1029/1999JC900086.

[44] X. N. Li, J. Zhang, Y. S. Dai, and X. Zhang, "Research on the enhanced performance of texture feature for sea ice drift monitoring based on gray level co-occurrence matrices," *Marina Sci.*, vol. 42, pp. 9–17, 2018, doi: 10.11759/hykx20170803001.

[45] R. M. Haralick, K. Shanmugam, and I. Dinstein, "Textural features for image classification," *IEEE Trans. Syst., Man Cybern.*, vol. SMC-3, no. 6, pp. 610–621, Nov. 1973, doi: 10.1109/TSMC.1973.4309314.

[46] D. G. Lowe, "Distinctive image features from scale-invariant keypoints international," *J. Comput. Vis.*, vol. 60, pp. 91–110, 2004, doi: 10.1023/B:Visi.0000029664.99615.94.

[47] J. Karvonen, M. Similä, and J. Lehtiranta, "SAR-based estimation of the Baltic sea ice motion," in *Proc. IEEE Int. Geosci. Remote Sens. Symp.*, 2007, pp. 2605–2608, doi: 10.1109/Igarss.2007.4423378.

[48] D. Demchev, V. Volkov, E. Kazakov, P. F. Alcantarilla, S. Sandven, and V. Khmeleva, "Sea ice drift tracking from sequential SAR images using accelerated-KAZE features," *IEEE Trans. Geosci. Remote Sens.*, vol. 55, pp. 5174–5184, Sep. 2017, doi: 10.1109/Tgrs.2017.2703084.

[49] M. Zhang et al., "Detection of sea ice drift based on different polarization data," *Laser Optoelectron. Prog.*, vol. 56, pp. 138–143, 2019, doi: 10.3788/LOP56.101008.

Chengzhi Sun received the B.Sc. degree in photogrammetry and remote sensing from Wuhan Technical University of Surveying and Mapping, Wuhan, China, in 1987, and the Ph.D. degree from the State Key Laboratory of Information Engineering Surveying, Mapping and Remote Sensing (LIESMARS), Wuhan University, Wuhan, in 2010.

He has served as the Chief Engineer of the ZY-3 Satellite Application System Project and Deputy Director of the Satellite Mapping Application Center of the National Administration of Surveying, Mapping and Geoinformation. He is currently the Chief Scientist and Professor with Nanjing University of Information Science & Technology. His main research areas include satellite mapping applications, as well as the overall design and engineering development management of remote sensing satellites.

Chao Wang received the B.S. degree in information engineering and the M.S. degree in communication and information system from the China University of Mining and Technology, Xuzhou, China, in 2007 and 2010, respectively, and the Ph.D. degree in computer application technology from the Hohai University, Nanjing, China, in 2014.

He is currently an Associate Professor with the School of Electronics and Information Engineering, Nanjing University of Information Science and Technology, Nanjing. His current research interests include remote sensing image processing and applications, machine learning, deep learning, and pattern recognition.

Yanli Yang received the B.S. degree in physical geography and resource environment from Guangdong University of Finance & Economics, Guangzhou, China, in 2019 and the M.S. degree in marine science from the Shanghai Ocean University, Shanghai, China, in 2022. She is currently working toward the Ph.D. degree in environmental remote sensing with the School of Remote Sensing and Geomatics Engineering, Nanjing University of Information Science and Technology, Nanjing, China.

Her current research interests include remote sensing image processing, sea ice motion.

Jian Li received the doctor's degree in remote sensing from Wuhan University, Wuhan, China, in 2015.

He was a Postdoctor with the School of Remote Sensing and Information Engineering, Wuhan University. He is currently an Associate Professor with Nanjing University of Information Science and Technology. His main research interests are ocean and coastal environment remote sensing and assessment.

Tao Xie received the M.S. degree from Guizhou University of Technology, Guiyang, China, in 2002, and the Ph.D. degree in electromagnetic fields and microwave technology from the Shanghai Jiaotong University, Shanghai, China, in 2005.

He was a Postdoctoral Fellow in oceanography and ocean remote sensing with the Bedford Institute of Oceanography, Dartmouth, NS, Canada. He is currently a Professor with Nanjing University of Information Science and Technology. His research interests include modeling of EM backscattering from ocean surface, ocean surface parameters retrieval from SAR imageries, oil spilling detection by SAR, and Arctic sea ice remote sensing.

Xuehong Zhang received the doctor's degree in remote sensing of resources and environment from Nanjing University, Nanjing, China, in 2012.

He was a Postdoctor with the School of Atmospheric Sciences, Nanjing University of Information Science and Technology. He is currently a Professor with Nanjing University of Information Science and Technology. His main research interests include coastal remote sensing and hyperspectral remote sensing.